Materials & Design 231 (2023) 112000

Contents lists available at ScienceDirect

Materials & Design

journal homepage: www.elsevier.com/locate/matdes

Nanoindentation creep of supercrystalline nanocomposites

Cong Yan [a], Büsra Bor [b], Alexander Plunkett [b], Berta Domènech [b,c], Verena Maier-Kiener [d], Diletta Giuntini [a,b,*]

[a] Department of Mechanical Engineering, Eindhoven University of Technology, The Netherlands
[b] Institute of Advanced Ceramics, Hamburg University of Technology, Germany
[c] ams-OSRAM International GmbH, ams OSRAM Group, Germany
[d] Department of Materials Science, Montanuniversität Leoben, Austria

HIGHLIGHTS

- The creep behavior of ceramic-organic supercrystalline nanocomposites is assessed for the first time, via nanoindentation.
- The organic phase, even though less than 10 wt%, plays a dominant role in the nanocomposites' deformation.
- Partial recovery of creep after unloading reveals that supercrystals feature both viscoelasticity and viscoplasticity.
- Ligands-facilitated rearrangement of the ceramic nanoparticles is proposed as dominating creep mechanism of supercrystals.
- The applicability of nanoindentation methodologies, single loading and continuous stiffness measurement, is analyzed.

GRAPHICAL ABSTRACT

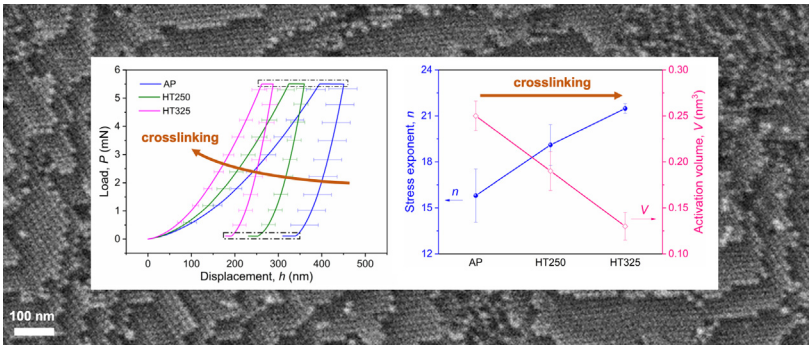

ARTICLE INFO

Article history:
Received 9 February 2023
Revised 25 April 2023
Accepted 11 May 2023
Available online 17 May 2023

Keywords:
Nanocomposites
Supercrystals
Nanoindentation
Creep

ABSTRACT

Supercrystalline nanocomposites (SCNCs) are inorganic-organic hybrid materials with a unique periodic nanostructure, and thus they have been gaining growing attention for their intriguing functional properties and parallelisms with hierarchical biomaterials. Their mechanical behavior remains, however, poorly understood, even though its understanding and control are important to allow SCNCs' implementation into devices. An important aspect that has not been tackled yet is their time-dependent deformation behavior, which is nevertheless expected to play an important role in materials containing such a distribution of organic phase. Hereby, we report on the creep of ceramic-organic SCNCs with varying degrees of organic crosslinking, as assessed via nanoindentation. Creep strains and their partial recoverability are observed, hinting at the co-presence of viscoelasticity and viscoplasticity, and a clear effect of crosslinking in decreasing the overall material deformability emerges. We rationalize our experimental observations with the analysis of stress exponent and activation volume, resulting in a power-law breakdown behavior and governing deformation mechanisms occurring at the organic sub-nm interfaces scale, as

* Corresponding author at: Department of Mechanical Engineering, Eindhoven University of Technology, The Netherlands.
E-mail address: d.giuntini@tue.nl (D. Giuntini).

https://doi.org/10.1016/j.matdes.2023.112000

rearrangement of organic ligands. The set of results is reinforced by the evaluation of the strain rate sensitivity via strain rate jump tests, and the assessment of the effect of oscillations during continuous stiffness measurement mode.

1. Introduction

Nanocomposites are a particularly promising material category when it comes to fostering new and targeted combinations of functional and mechanical properties, but their controlled processing remains a challenge [1]. Supercrystalline nanocomposites (SCNCs) show great potential in this regard, since their peculiar nanostructure offers unique opportunities for the fine-tuning of their design at the nano- and micro-scale, and thus of their macroscopic behavior [2,3]. SCNCs consist of inorganic nanoparticles (NPs) that are surface-functionalized with organic ligands and architected into long-range ordered structures. These are reminiscent of atomic crystal lattices, even though at a characteristic scale that is typically two orders of magnitude larger, and are thus called superlattices [3]. Two key strategies to achieve these nanostructures (often of the face- or body-centered cubic type, FCC or BCC) are the organic functionalization of the NP cores, which prevents their uncontrolled aggregation during processing, and a narrow NP size distribution [4,5]. The combination of nano-sized building blocks and their periodic arrangement in superlattices with ultra-thin inter-NP spacings leads to a wide spectrum of emergent collective properties – electronic, optical, magnetic, thermal, and more. Furthermore, SCNCs present a strong analogy with biomaterials, due to their nanostructured and hierarchical architectures consisting of a tailored mix of inorganic–organic constituents, and one can thus foresee potentially achieving enhanced mechanical properties for applications in e.g. bioimplants, additional to those in battery electrodes, catalysts and optoelectronic devices enabled by their functional properties [3,6–10].

In all these instances, then, understanding and controlling the mechanical behavior of this new material category acquires paramount importance. The mechanical characteristics of SCNCs are, however, still largely unexplored. Among the several factors affecting their mechanical properties (NP size [11–13], packing density [13], ligand-NP binding strength, interactions among ligands [11,13], and between ligands and solvent the NP system is stabilized into [14]), the organic ligands play a key role. By inducing their crosslinking, for instance, it has been shown that a remarkable increase in the SCNCs strength, hardness, stiffness, and even fracture toughness, can be achieved [4,5,11–19]. On the other hand, the presence of an organic phase leads to the presence of time-dependent features in their mechanical response [17,20]. This is expected also considering again the analogy with organic-mineral biomaterials, for which creep has been observed and characterized (e.g. enamel [21,22], bone [23], intervertebral disc [24]). Creep occurs when testing SCNCs [17], but the underlying deformation mechanisms remain to be unveiled.

Uniaxial creep testing is relatively cumbersome to implement when it comes to SCNCs, since their production in large sizes is still quite challenging. Nevertheless, creep testing via instrumented indentation has progressively been perfected since its initiation in the 1970s [25], and nanoindentation has become a reliable, efficient and well-established method to evaluate the creep behavior of nano- and micro-structured materials [26], such as nanocrystalline metals [27–29], ceramics [30,31], amorphous materials [32], polymers [33] and biomaterials [21–24]. Even though the stress field's distribution and magnitude induced via indentation can lead to deviations from uniaxial testing [26,34], many analyses have however shown a very good agreement between the creep behavior measured with the two testing methods [27,32,35].

There is an additional important aspect to consider when it comes to nanoindentation creep. Although indentation creep tests are typically carried out under single-loading mode (i.e. quasi-static load), they can also be conducted in the so-called continuous stiffness measurement (CSM) mode [36]. Under CSM mode, a harmonic load with small amplitude and high frequency is superimposed on the quasi-static load, enabling a continuous estimation of contact stiffness, and thus a more accurate estimation of elastic modulus and hardness, and reducing the influence of thermal drift, which represents a major concern in creep studies [37–40]. These super-imposed oscillations can, however, lead to alterations of the measured mechanical behavior [41,42]. Potential sources of error have been identified (underestimation of applied load, displacements or contact stiffness, and loss of contact in the initial test stages) and both preventive strategies and corrections have been proposed [43] – such as not applying this method to materials with large *E/H* ratios to avoid alterations in the contact stiffness due to local plasticity [44]. Nevertheless, a great variety of deformation phenomena can still occur during CSM-based tests, such as fatigue-associated failure, softening associated with dislocation nucleation in metallic materials, or hardening associated with strain rate sensitivity [45–48]. When it comes to SCNCs, given the peculiarity of their tightly packed arrangement and the extreme confinement of the organic ligands (in the same length-scale of the harmonic oscillations), the effect of the CSM testing mode cannot be directly associated with any of these mechanisms, and thus calls for a separate analysis.

Here, the creep behavior of SCNCs is characterized and analyzed under quasi-static and CSM loading modes. The deformation is assessed for both initial and secondary (quasi-static) creep regimes, and for its recoverability. Classic creep concepts, i.e. stress exponent (as reciprocal of strain rate sensitivity, also tested via strain rate jump tests) and activation volume, are critically applied to this novel material category, and a new creep mechanism, i.e. organic-facilitated NP movement, achieved via the rearrangements of the organic ligands in the sub-nm inter-particle spacings, is proposed for SCNCs.

2. Materials and methods

2.1. Samples preparation

The supercrystalline nanocomposites consist of iron oxide (magnetite, Fe_3O_4) NPs, surface-functionalized with oleic acid (OA) and initially suspended in toluene (Fraunhofer CAN GmbH, Hamburg, Germany). Starting from these building blocks, the formation of the supercrystalline structure is induced by self-assembly via solvent destabilization [17,18]. The NP suspension (40 mg/mL) is poured into a die-punch assembly (14 mm diameter), and placed into a desiccator, in which the atmosphere is then enriched with ethanol, acting as destabilization agent upon slow diffusion into the NP colloidal suspension. The self-assembly process lasts ~15 days. The dry SCNCs ae then recovered by removal of the supernatant with a pipette. The samples are dried for 24 h under ambient conditions followed by 2 h under vacuum. By

means of a second punch they are pressed uniaxially (in a rigid die) at 150 °C and with 50 MPa, to obtain bulk cylindrical pellets, ~4 mm thick. The pellets are then cut into three portions. One is left as-pressed (AP), while the other two are subjected to a heat treatment (HT) at 250 and 325 °C under nitrogen (N_2) atmosphere (heating and cooling ramps 1 °C/min, holding time 18 min). The heat treatment induces the crosslinking of the organic ligands, and in turn a boost of the SCNCs' mechanical properties [4,17–19,49]. The different types of samples (AP, HT250, HT325) are then fixed on SEM stubs with silver glue and embedded into cold-curing acrylic resin (Scandiquick, Scan-DIA, Hagen, Germany) to test the cross-section of the pellets. The samples' surface is polished with SiC paper and then diamond suspensions, down to a roughness of 50 nm.

2.2. Composition and nanostructure characterization

To quantify the organic content in the 3 different materials (AP, HT250 and HT325), thermogravimetric analysis (TGA) is conducted in a Mettler Toledo TGA/DSC1 STARe System (Mettler Toledo, UK), from 25 to 900 ℃ with a heating rate of 5 ℃/min, under nitrogen (N_2) atmosphere. The indents are observed by scanning electron microscopy (SEM, Zeiss 55-VP, Zeiss, Germany) at 2 kV, to verify that the indents are in supercrystalline areas (avoiding defects) and that severe damage has not been induced around the indents. Topographic measurements are conducted via atomic force microscopy (AFM, NanoScope IV, Dimension 3100 of Digital Instruments, USA), with a 0.5 Hz scanning speed.

2.3. Nanoindentation

The nanoindentation tests are performed in an G200 system (KLA, formerly Agilent, USA) at room temperature, with a diamond Berkovich tip (Synton-MDP, Switzerland), chosen for its geometrical self-similarity [29] and wide use in creep tests. The single-loading mode (quasi-static) tests consist of five phases: I) loading; II) creep; III) unloading; IV) backcreep (a low-load, 2% of the maximum load, holding step aimed at investigating creep recoverability); V) thermal drift measurement (see the inset of Fig. 2 (a)). For I and III, a rate 0.2 mN/s is selected, to guarantee a fast loading/unloading, as well as to avoid overshooting the prescribed maximum load. During II and IV, the holding time is 1000 s. The maximum loads are 2.5, 4, 5.5 and 10 mN, corresponding to 200–500 nm depths, to ensure that the indenter penetrates the sample for a number of layers of nanoparticles representative of the bulk material, as well as to avoid the occurrence of cracking and chipping damage, based on preliminary tests and previous work [17]. The backcreep (IV) load of 2% of the maximum load has been selected to guarantee reliable displacement measurements while minimizing its effect on creep recovery, in accordance with the recommendations in [21]. The holding time for thermal drift measurement (V) is set as 75 s. The choice of conducting tests in load-control mode, instead of displacement-control, is due to the precise target control and the minimization of the influence of thermal drift that load-control allows [21,27–29], but tests in displacement-control mode were also conducted to check on the general applicability of the test results. The CSM loading mode is also employed in this study, for 2 purposes: i) measuring the SCNCs' elastic modulus (E) and hardness (H) (constant strain rate of 0.05 s^{-1} and maximum depth of 300 nm [17], still Berkovich tip); ii) investigating the influence of oscillations on the creep deformation, with a harmonic amplitude of 2 nm and a frequency of 45 Hz. The tests under CSM mode consist of the same 5 steps. At least 12 indents were performed for each load and measurement mode, at a distance of 30 μm from each other. To eliminate the effect of thermal drift during long-term indentation experiments, a multi-approach analysis

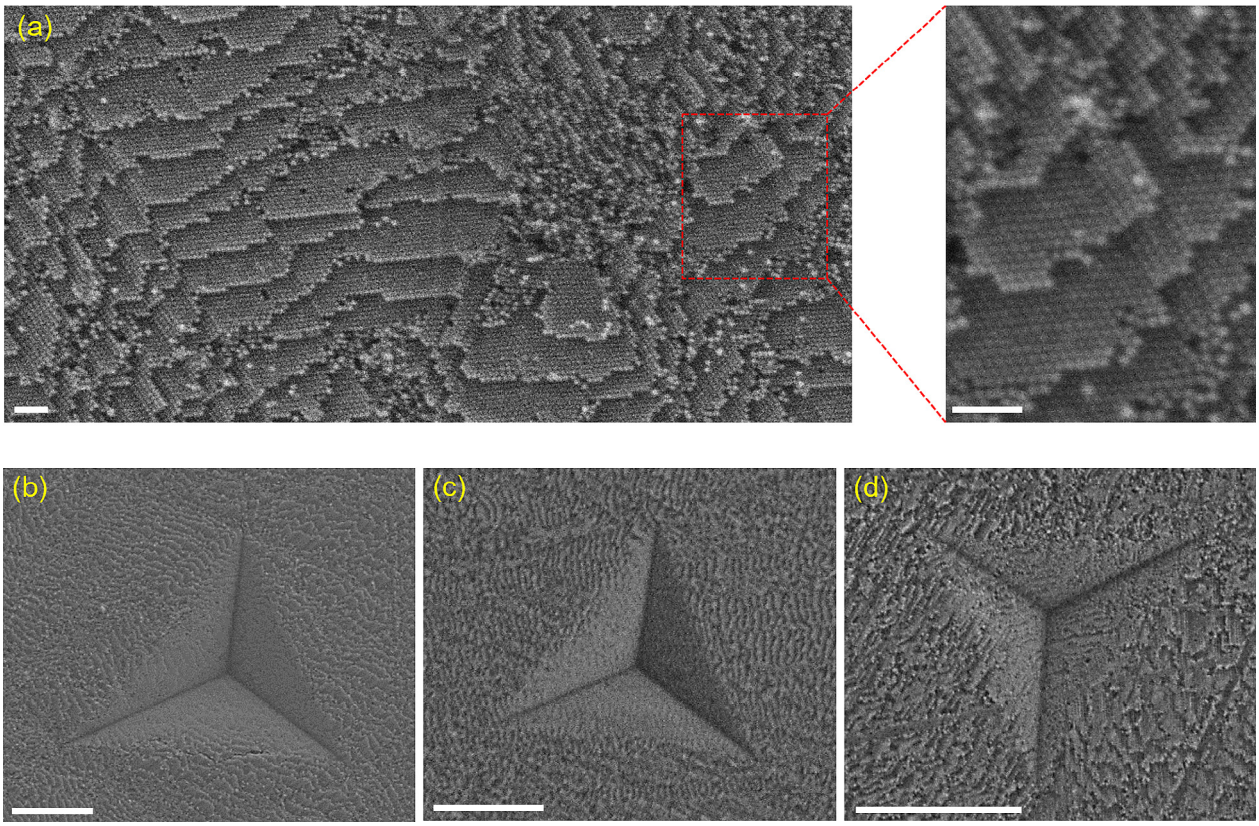

Fig. 1. Nanostructure and indents in SCNCs. (a) Fracture surface in AP sample, with view of the periodic NP arrangement in the magnified image; (b) – (d) indents in different samples obtained with 5.5 mN load: b) AP; c) HT250; d) HT325. All images are SEM micrographs. Scale bars: 100 nm in (a), 1 μm in (b) – (d).

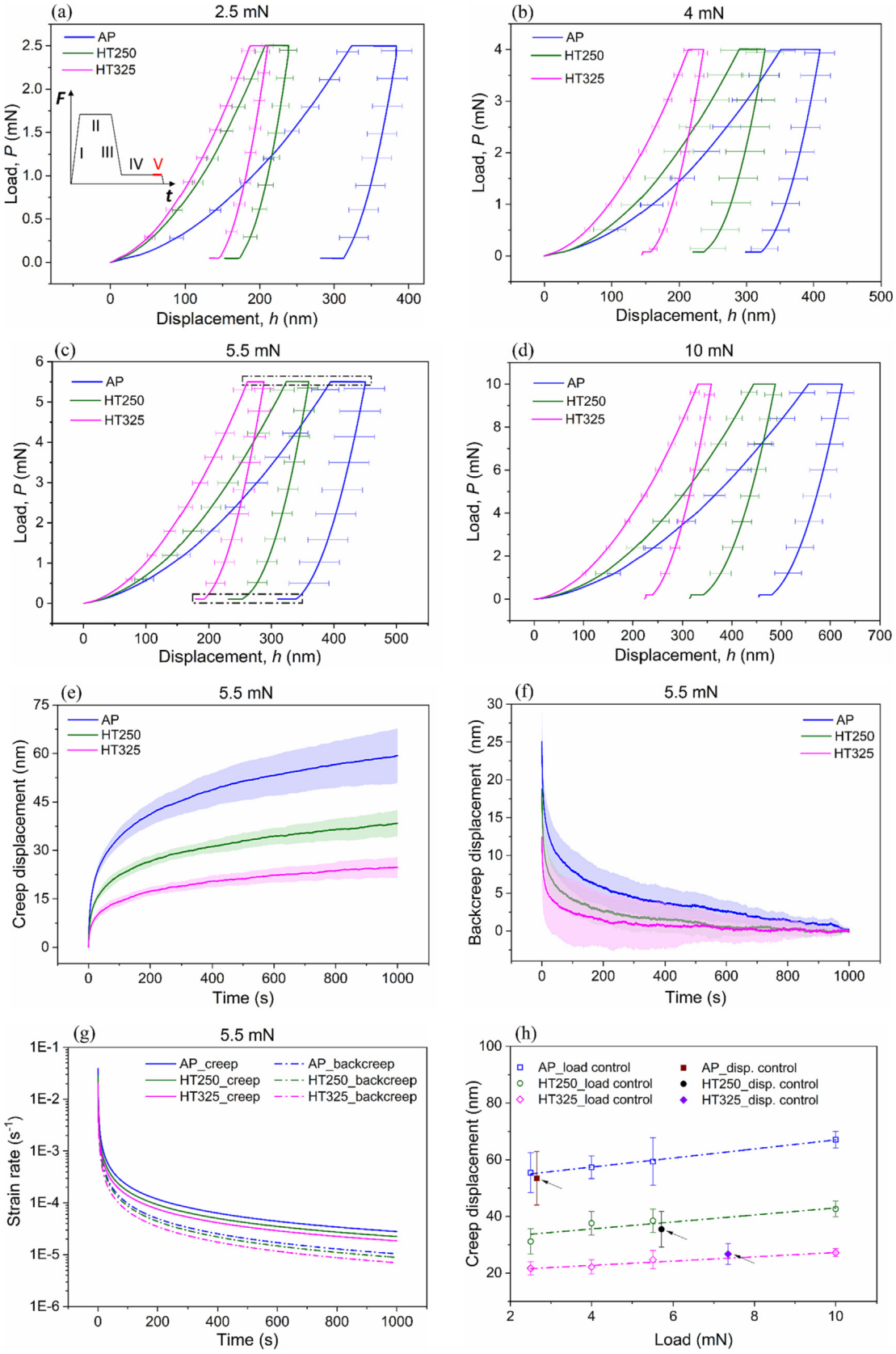

Fig. 2. Analysis of nanoindentation creep deformation of SCNCs. (a) – (d) Load-displacement curves under different loads: (a) 2.5 mN; (b) 4 mN; (c) 5.5 mN; (d) 10 mN. The inset in (a) displays the loading scheme (I – loading tamp; II – creep; III – unloading ramp; IV – backcreep; V – thermal drift measurement); (e), (f) Evolution of creep/backcreep displacements in 5.5 mN tests (marked by dashed boxes in (c)): (e) creep; (f) backcreep. The shading bands indicate the standard deviation. (g) Strain rates in 5.5 mN tests during creep and backcreep; (h) Comparison of creep displacements as obtained in load-control (hollow symbols) and displacement-control mode (solid symbols, indicated by arrows) creep tests.

is conducted, as explained in Appendix A. The initial thermal drift rate is set as 0.05 nm/s to enable the start of the creep tests, and during the tests the actual drift values are below 0.02 nm/s, as shown in Fig. A1. The tip calibration is performed on silica.

3. Results and discussions

3.1. Nanostructure, composition and mechanical properties of supercrystalline nanocomposites

The starting constituents and the final nanostructure of the SCNCs are characterized by transmission and scanning electron microscopy (TEM, SEM) and small angle X-ray scattering (SAXS), see SI Section S1 and Fig. S1. The NP radius is 7.4 ± 0.8 nm according to SAXS (Fig. S1(c)). SAXS also reveals the face-centered cubic (FCC) superlattice of the self-assembled SCNCs for all three types of samples (Fig. S1(d)), with superlattice constants of 22.8 ± 0.04 nm for AP, 22.9 ± 0.03 nm for HT250 and 21.9 ± 0.12 nm for HT325, corresponding to interparticle distances (*ID*) of 1.2 ± 0.03 nm, 1.3 ± 0.02 nm and 0.6 ± 0.09 nm, respectively, as reported in Table 1. Considering the length of the totally extended OA molecule (~2 nm), these values suggest that the organic ligands are interdigitated and/or bent at the interfaces between NPs. The organic content is measured by TGA, as summarized in the same Table 1 (see also SI Section S2 and Fig. S2). Superlattice shrinkage, typically reported for heat-treated SCNCs [49], is only observed in the HT325 case, while the HT250 sample has only a minor reduction of the organic content with respect to the AP counterparts. This is because the reactions induced by the heat treatment and that lead to strengthening and ID reduction proceed at different rates, and thus at 250 °C strengthening is achieved without significant shrinkage, while at 325 °C both are detected [19]. Based on the TGA-measured organic content in AP samples, the OA grafting density on the NP surface is also obtained, as ~2.4 molecules/nm^2 (see SI Section S3). This is then compared with the maximum theoretical grafting density, i.e. the amount of organic ligands required to form a full monolayer on the NP surfaces. Assuming that the ligands are oriented perpendicular to the NP surface and that the entire NP surface is available for the binding of ligands, the theoretical grafting density is then determined as 4.8 molecules/nm^2 (considering that the area of the OA anchoring group to the NP is 0.21 nm^2) [50]. It should be noted that this theoretical value provides an upper bound of grafting density, since the NP surfaces are likely to have binding sites that do not allow their complete coverage with ligands, and that at the same time TGA can underestimate the overall organic content, due to the fact that some residual carbon can remain in the measured samples, on the NP surfaces [51]. Nevertheless, the theoretical value is much larger than the experimental one, making it reasonable to assume that the superlattice interstitial sites are empty.

The SCNCs' elastic modulus and hardness are measured via nanoindentation in CSM mode (see SI Section S4 and Fig. S3) and the corresponding values are also summarized in Table 1. With increasing heat treatment temperature, crosslinking is induced, and covalent bonds are formed in-between adjacent OA molecules, leading to a high-strength network holding the material together [4,19]. Therefore, the elastic modulus and hardness are gradually enhanced, and this increase is particularly remarkable for the HT325 sample (58% increase of elastic modulus and 113% increase of hardness with respect to the AP case). For the HT250 sample, the enhancement is less pronounced, as a result of slight decrease of organic content and less pronounced crosslinking. These *E* and *H* values are remarkably high for ceramic-organic nanocomposites, and especially for supercrystalline materials, which usually feature the elastic moduli in the 1 – 20 GPa range and hardness around 40 – 450 MPa [12].

The typical SCNCs nanostructure is shown in Fig. 1(a), displaying a fracture surface in the AP material, which is representative of all samples (the differences among them are not detectable at this resolution). The long-range order arrangement of the NPs is visible. The superlattice orientation is not uniform throughout the cm-sized samples, thus rendering the SCNCs polysupercrystalline, and the probed mechanical properties can in turn be considered isotropic. The morphologies of indents obtained with a 5.5 mN load are shown below, in Fig. 1(b) – (d). All indents are analyzed at the SEM, confirming that the wide majority have been performed in supercrystalline domains, and not in localized defect-affected or amorphous regions. The varying superlattice orientations can also be observed in these micrographs. Indentation-induced damage, such as cracking and chipping, is not detected in the indents performed with 5.5 mN, and it is then reasonable to conclude that no damage is induced by indenting at lower loads (i.e. 4 mN and 2.5 mN). The indents obtained at 10 mN are also examined, see SI Fig. S4, whereby slight damage can only be seen in a few indents in AP and HT250 samples, but none in the HT325 sample. The data relative to the 10 mN load is thus also considered in the following analysis.

3.2. Creep occurrence

Load-displacement nanoindentation curves obtained in 2.5, 4, 5.5 and 10 mN tests are shown in Fig. 2(a) – (d). For all applied loads, the maximum displacements gradually decrease from AP to HT325 SCNCs, as expected thanks to the crosslinking-associated enhancement of the mechanical properties. Creep occurs during the holding at maximum load, while recovery occurs during the backcreep stage, as marked in Fig. 2(c). To compare the evolution of creep and backcreep displacements of different samples, these are displayed for the 5.5 mN case in Fig. 2(e) and (f), respectively, and in SI section S6 for the three other loads. In Fig. 2(e), one can observe that creep displacements first increase quickly and then slow down. The higher the heat-treatment temperature, the smaller the overall creep displacements, indicating that creep resistance is enhanced by the ligands' crosslinking. The backcreep displacements in Fig. 2(f) show a similar trend, initially dropping sharply and then slowing down. The tests under different loads (Fig. S5) share the same features. Note that the backcreep displacements approaching zero indicate that creep recovery has a negligible influence on the thermal drift measurements.

Strain rates are also analyzed, to evaluate the difference of deformation rate between creep and backcreep. The empirical power-law expression $h(t) = a + b * t^c$ is adopted to fit the results [38], and the strain rate is then calculated as:

Table 1
Superlattice parameters (superlattice constant and interparticle distance), organic content and mechanical properties (elastic modulus and hardness) of the tested supercrystalline nanocomposites (SCNCs).

	Superlattice constant, *a* (nm)	Interparticle distance, *ID* (nm)	Organic content (wt%)	Elastic modulus, *E* (GPa)	Hardness, *H* (GPa)
AP	22.8 ± 0.04	1.2 ± 0.03	8.0	37.9 ± 2.6	1.97 ± 0.24
HT250	22.9 ± 0.03	1.3 ± 0.02	7.3	43.1 ± 4.2	2.40 ± 0.38
HT325	21.9 ± 0.12	0.6 ± 0.09	5.5	59.8 ± 6.2	4.19 ± 0.52

$$\dot{\varepsilon} = \frac{\dot{h}}{h} = \frac{dh/dt}{h} \quad (1)$$

where h is the total displacement [32]. The evolution of strain rates during creep and backcreep is shown in Fig. 2(g). The strain rates decay quickly, both for creep and backcreep, and tend to a quasi-constant value, with the backcreep strain rates consistently smaller than those of creep, by a factor of ~3. As typical in nanoindentation tests, due to the multiaxial stress, a fully steady state (constant strain rate) is not reached [26], so we will refer to this later creep stage as quasi-secondary (or quasi-steady state).

The varying maximum displacements in the different materials (Fig. 2(a) – (d)) indicate that for each case different volumes are involved by the indentation tests when the same load is applied. To verify whether the volume of deformed material impacts creep deformation, displacement-control (300 nm) creep tests were also conducted, keeping all other parameters unchanged. It should be noted that previous works have revealed the occurrence of compaction in SCNCs [17,49], implying that even in displacement-control tests one cannot attain exactly equivalent volumes of material affected by the indentation load, but it is still reasonable to assume that such volumes are sufficiently close to each other when the indentation depth is kept constant. The comparison of creep displacements between load-control and displacement-control creep tests is summarized in Fig. 2(h). The creep displacements under load-control tests exhibit a linear relationship with the load, with which the data from displacement-control tests is aligned, indicating that no significant difference can be detected between load-control and displacement-control creep tests, and that the influence of different indented volumes can thus be neglected.

4. Recoverability of creep deformation

Due to the presence of an organic phase in the SCNCs, and the typically associated viscous material behavior, creep recovery, at least partial, is analyzed. The same phenomenon has indeed been consistently observed in biomaterials (enamel [21], intervertebral disc [24]) and polymers [52,53]. For instance, He et al. reported that almost 40% of creep deformation in enamel is recovered during backcreep, indicating that both viscoelastic and viscoplastic deformation occur [21], while certain polymers can achieve complete recovery [52]. The displacements during creep and backcreep under the four different loads are compared in Fig. 3(a), where one can see that backcreep displacements are consistently smaller than creep ones, with the ratios of backcreep to creep displacements ranging from 40% to 50%, similarly to the values reported in [21], indicating that creep deformation does not fully recover during backcreep. This only partial recovery is associated with a relatively low organic content, and especially the high confinement of the organic ligands in ultra-thin inter-NP spacings, in which the OA molecules are anchored to the NP surfaces, likely interdigitated and sometimes also crosslinked.

From Fig. 2(g) one can notice, however, that the strain rate during backcreep does not reach zero, and it might thus keep proceeding after nanoindentation. AFM measurements are then performed several weeks after the nanoindentation tests, on selected indents, to verify whether the recovery continues after the indenter's withdrawal.

Fig. 3(b) – (g) show the resulting topography maps and depth profiles. The "bumpy" surfaces (Fig. 3(b), (d), (f)) along the side faces of the indents suggest that recovery continues after the tip is retracted (see e.g. the area marked by the dashed box in Fig. 3 (b)). The residual depths measured via AFM (Fig. 3(c), (e), (g)) are then compared with those resulting from nanoindentation. For AFM, the intersection of the three scanning lines shown in Fig. 3 (c), (e) and (g) is taken as residual depth marker. The difference between residual depth (AFM) and final nanoindentation depth is the displacement recovered after nanoindentation, as summarized in Table 2 for selected representative indents. The recovered displacements are still smaller than creep displacements, indicating that recovery is not complete even several weeks after nanoindentation. It thus appears that viscoelasticity and viscoplasticity both occur during creep, although visco-plasticity only accounts for 20–30% of the overall deformation. The Kohlrausch-Williams-Watts (KWW) model, usually adopted to describe viscoelastic stress evolution during constant load holding [54], also fails to describe the stress evolution in the case of SCNCs. Instead, an expression with double exponential terms describes well this stress evolution ($R^2 > 0.99$), confirming that creep deformation is not solely viscoelastic, and that viscoplastic deformation also occurs (see SI Section S7 and Fig. S6).

5. Initial creep

Based on the results in Fig. 2, one can identify two stages of deformation during the load holding stage. To distinguish from the case of uniaxial creep testing, these two stages of nanoindentation creep are termed initial creep and quasi-secondary creep. The latter term is chosen to underline that in nanoindentation a fully steady state cannot be reached. By integrating the strain rates obtained from Eq. (1), the strain evolution during holding can be obtained. The outcomes are shown in Fig. 4(a) – (d) (note that the initial strain is set back to zero to focus on creep strains only). This creep strain refers to the local deformation near the indenting tip, and it increases with indentation displacement. It should not be confused with the representative strain of ~8%, which is associated with the geometrical self-similarity of the Berkovich tip, and as such independent from the indentation displacement. The same trend can be found in all plots: the largest strains occur in AP SCNCs, the smallest ones in HT325 samples, with intermediate values in HT250 samples, verifying that crosslinking enhances resistance against creep. An attempt is made to identify the transition point between initial and quasi-secondary creep on the strain–time curves. Based on the definition of steady-state creep, strain should have a linear relationship with respect to time. A linear fitting is thus performed from the end of the strain–time curves, and the transition is set on the point where the linear fitting values deviate from the experimental ones by 2% [55], as indicated by the star symbol on the curves. We can then separately analyze initial and quasi-secondary creep, respectively.

The deformation during primary creep usually proceeds quickly before reaching steady-state creep [33]. If the strain during primary creep exceeds 2×10^{-3}, the evolution of strain can be described by a power-law model, i.e. $\varepsilon = Bt^a$, where B and a are constants depending on the material, with the time exponent a indicating the decay rate of the creep strain [56]. This model is applied to the initial creep data, and it is found that the experimental results match the model very well, which also implies that the method to determine the transition point is reasonable. The deformation during primary creep is much larger than that associated with the following creep stage, due to its high deformation rate [33]. More than 80% of the deformation is observed during initial creep, see SI Section S8 and Table S1, indicating that initial creep dominates the total creep deformation.

6. Quasi-secondary creep and underlying mechanisms

Even though accounting for a smaller part of the overall creep deformation, the secondary stage can shed light on the mechanisms of creep deformation. The strain rate and stress during

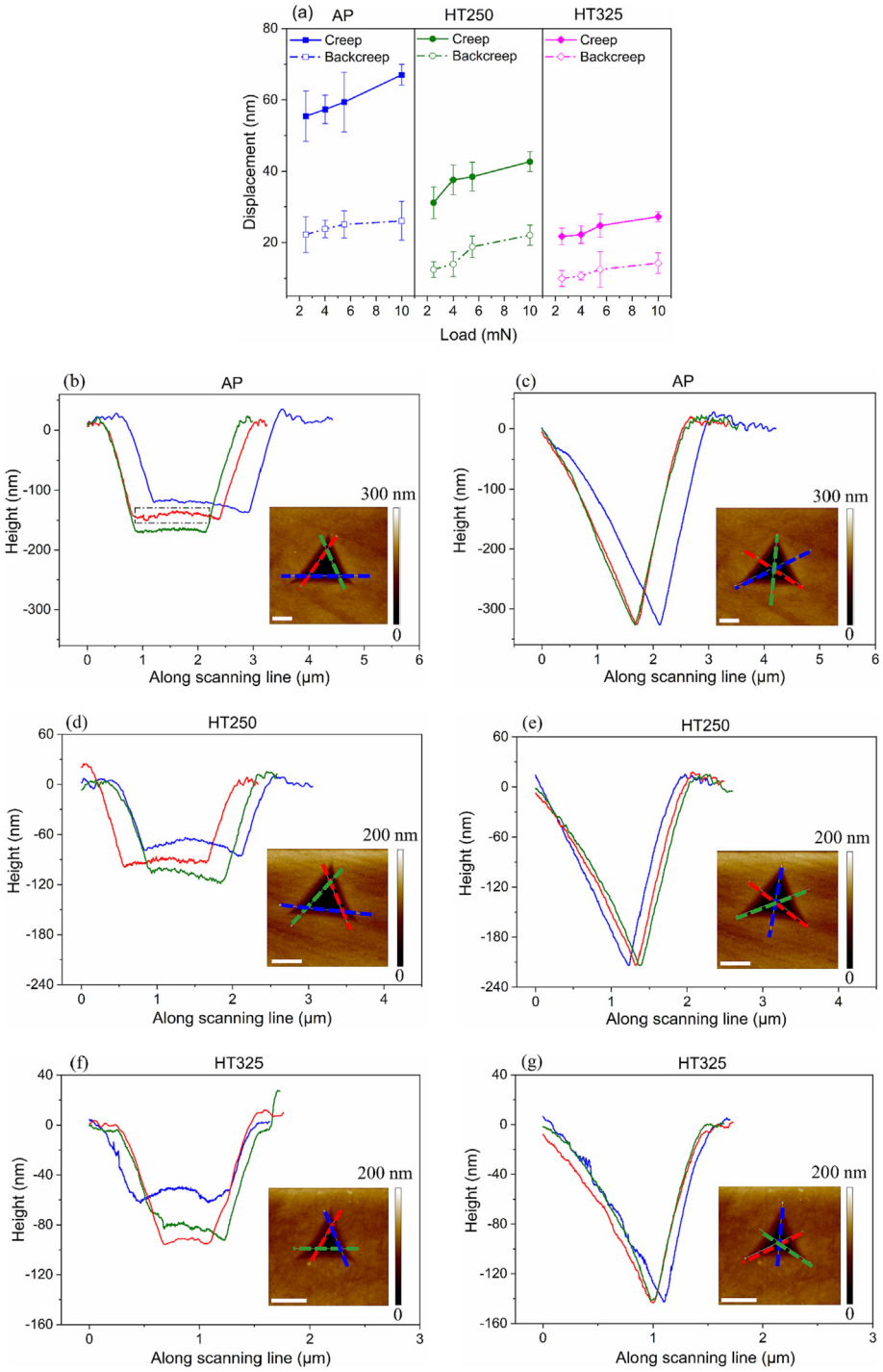

Fig. 3. Creep recovery analysis via nanoindentation and AFM. (a) Creep and backcreep displacements under different loads, as recorded by the nanoindenter. (b) – (g) Depth profiles along corresponding scanning lines in AFM topography maps, verifying the occurrence of recovery after nanoindentation: (b) – (c) AP sample; (d) – (e) HT250 sample; (f) – (g) HT325 sample. The bottom sections of the profiles in (b), (d), (f) display a somewhat round morphology (marked by a dashed box in (b)), hinting at the occurrence of recovery. The profiles in (c), (e), (g) show the depth variation along different scanning lines in AFM topography maps, adopted to determine the residual depth after nanoindentation, which is then compared with the depth recorded by nanoindentation to quantify the overall recovery. Scale bar is 1 μm in the AFM topography maps.

Table 2
Creep deformation recovery based on nanoindentation and AFM.

	Recovery after nanoindentation (nm)	Recovery during backcreep (nm)	Total recovery (nm)	Creep displacements (nm)	Total recovery (%)
AP	28	20	48	60	80%
HT250	16	12	28	40	70%
HT325	1	16	17	21	81%

Note: Total recovery = recovery during backcreep + recovery after nanoindentation. Nanoindentation has a resolution of 0.01 nm while AFM has a 0.1 nm resolution. Here we rounded both up to integer values.

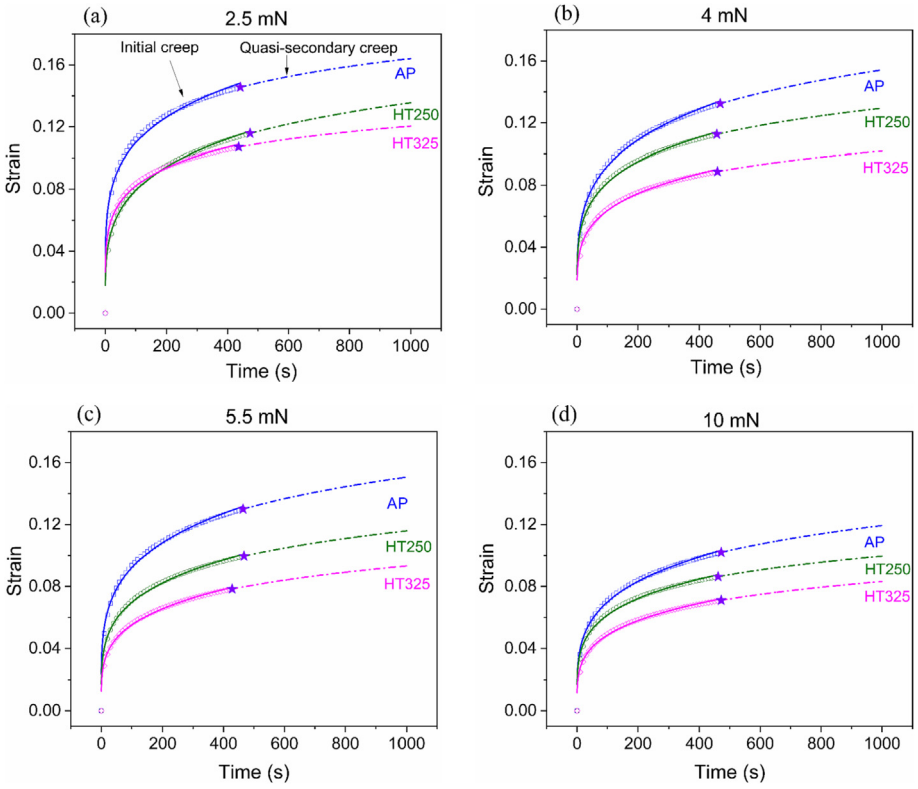

Fig. 4. Identification of initial and quasi-secondary creep on the strain–time curves: (a) 2.5 mN; (b) 4 mN; (c) 5.5 mN; (d) 10 mN. The first segment of the curves, plotted as scatter squares, represents initial creep, while the second segment of curves, plotted in dashed lines, marks the quasi-secondary creep. The shift between the two regimes is marked by transition points, indicated by star symbols. A power-law model fits the strain during initial creep (solid lines) with a high correlation coefficient ($R^2 > 0.98$).

steady state creep are usually correlated via an empirical power-law equation:

$$\dot{\varepsilon} = A\sigma^n \exp(-\frac{Q}{RT}) \tag{2}$$

where $\dot{\varepsilon}$ is strain rate, A is a constant associated with microstructural features, σ is the stress, n is the stress exponent, Q is the activation energy of creep deformation, R and T are the ideal gas constant and absolute temperature, respectively [28,57]. It is widely accepted that the stress exponent (n) is an indicator of creep mechanisms, i.e. $n = 1$ for diffusion creep, $n = 2$ for grain boundary sliding, $n = 3 – 7$ for creep related to dislocation activity, $n > 7$ for power-law breakdown [57–59].

Several previous studies have revealed that the stress exponent (n) typically coincides in the cases of nanoindentation and uniaxial tension creep, suggesting that similar creep mechanisms occur, although a difference can sometimes still exist due to the high stress concentrations associated with nanoindentation [27]. As anticipated above, it has also been reported that in nanoindentation creep a fully steady state is generally not reachable [26], but since the strain rates in this study ($\sim 10^{-5}$ s^{-1}) are comparable to or even smaller than several other reported strain rates where Eq. (2) has been applied to derive the stress exponent (n) [28,60], it is reasonable to analyze such quasi-steady-state creep mechanisms within this framework.

6.1. Stress exponent and strain rate sensitivity

The stress exponent (n) can be obtained as $n = \frac{\partial \ln \dot{\varepsilon}}{\partial \ln \sigma} = \frac{\partial \ln \dot{\varepsilon}}{\partial \ln H}$ from Eq. (2), where σ is usually made equivalent to hardness (H) data in nanoindentation creep. Hardness is calculated as

$$H = \frac{P}{A_C} \tag{3}$$

where P is the load and A_C is the projected contact area [32]. The function of contact area A_C is shown in the Appendix, Eq. (A4). A negligible influence of indentation size effect on the strain rate sensitivity was verified in [39], and thus here it is reasonable to neglect this effect on the stress exponent (reciprocal of strain rate sensitivity). The stress exponent (n) is usually computed by linear fitting of strain rate and hardness in logarithmic plots, as shown in Fig. 5(a) – (d). By averaging the stress exponents obtained in the tests under the four different loads, n is determined as 15.80 for AP SCNCs, 19.10 for HT250 and 21.48 for HT325, all of which are>7, associated with the occurrence of power-law breakdown. Power-law breakdown indicates that the stress exponent is no longer constant with changes in applied stress, increasing with rising stress or strain rate [61]. However, the linearity between $ln\dot{\varepsilon}$ and lnH still appears to be valid in Fig. 5(a) – (d), perhaps due to the limited data range, which does not extend enough to reflect the loss of linearity. Meanwhile, n exhibits an increasing trend with heat-treatment temperature, as shown in Fig. 5(e).

Power-law breakdown is related to the high stresses induced by the nanoindenter, and signals the presence of very high creep strain rates. A threshold value above which power-law breakdown occurs is found in $10^{-3}G$, with G shear modulus of the material [62]. The SCNCs shear modulus (G) can be obtained from the Young's modulus (E) as $G = E/2(1+\nu)$, assuming the SCNCs as homogeneous and isotropic. The Poisson's ratio ν is taken as 0.34, as previously derived via FEM for HT325 sample and here extended to all cases [63]. The representative stress under the indent (assumed as average over the hydrostatic and plastic sub-indent zones) is

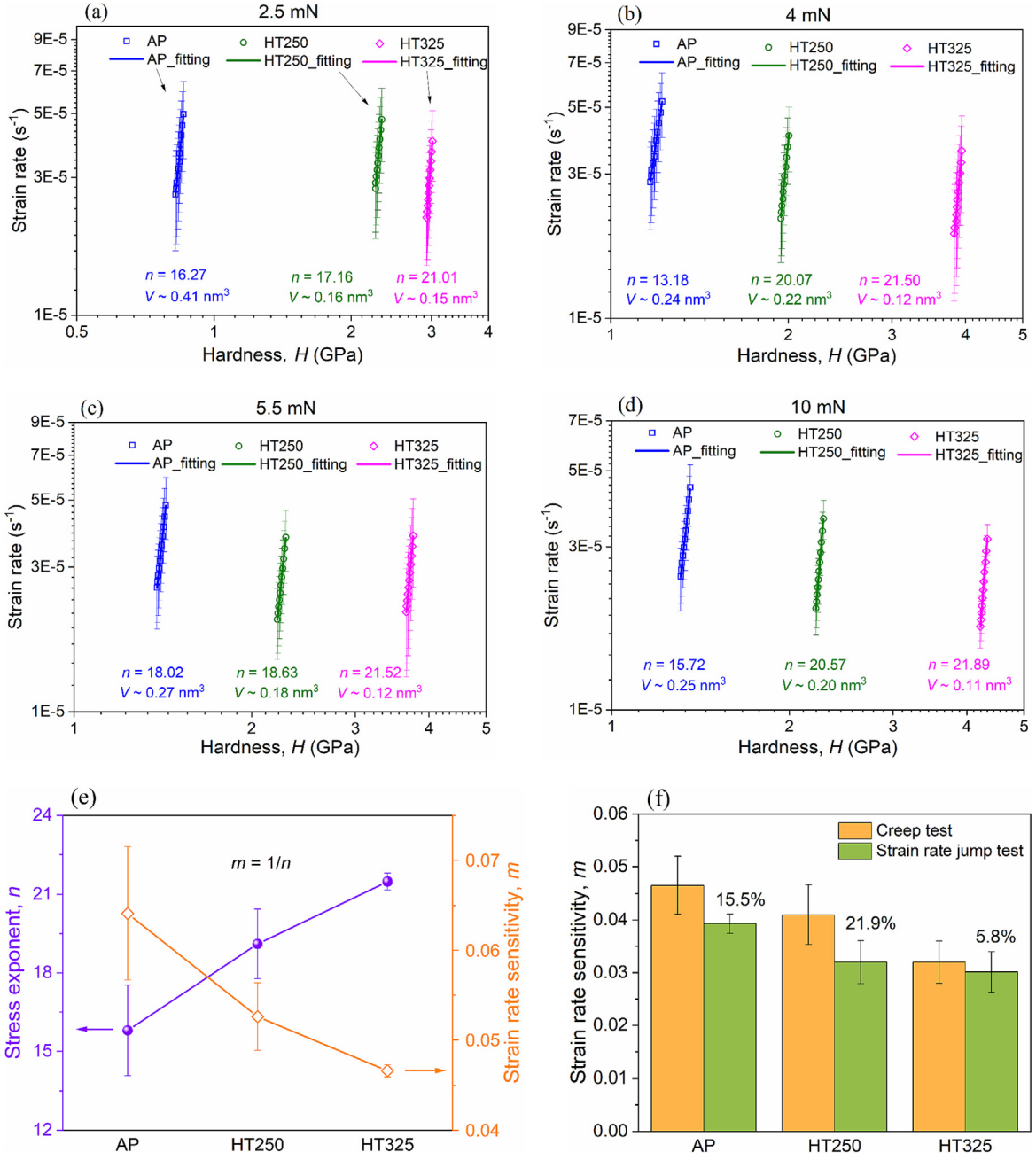

Fig. 5. Relations of logarithmic strain rate vs. logarithmic hardness during creep holding, the slope of which corresponds to the stress exponent (n): (a) 2.5 mN; (b) 4 mN; (c) 5.5 mN; (d) 10 mN; The activation volume (V) is also marked in the plots, corresponding to the slope of logarithmic strain rate vs. linear hardness as suggested by Eq. (5). The relevant plots can be found in Fig. S8. Note that only the test data relative to the secondary creep stage is shown here. (e) Comparison of the averaged n over the different loads for the three types of SCNCs, with the corresponding strain rate sensitivity (m = 1/n). (f) Comparison of strain rate sensitivity (m) obtained via creep and strain rate jump tests. The % indications above the columns indicate the difference of m as measured in these two tests, both carried out under CSM mode.

Table 3
Threshold stress values for power-law breakdown onset and representative stress beneath the indents.

	Shear modulus, G (GPa)	Threshold value (GPa)	Representative stress (GPa)			
			2.5 mN	4 mN	5.5 mN	10 mN
AP	14.1	1.41×10^{-2}	0.27	0.39	0.46	0.44
HT250	16.1	1.61×10^{-2}	0.75	0.65	0.74	0.74
HT325	22.3	2.23×10^{-2}	0.98	1.37	1.24	1.40

estimated from Tabor's law as $\sigma_r = H/C$, where C is a constraint factor, typically 1 – 3 depending on which regime (elastic/elasto-plastic/plastic) the deformation is in [64]. Here, C = 3 is adopted, and slight changes of C do not significantly impact the estimation. The results are summarized in Table 3. Compared with the threshold values calculated based on G, all the estimated representative

stresses are larger by at least one order of magnitude, confirming that the occurrence of power-law breakdown is expected.

Large stress exponents ($n > 7$) have also been reported in creep tests of UFG (ultrafine grained)-Al [37], UFG-Au [38], nanocrystalline Ni [26] and high entropy alloys [29]. All these tests were also performed with a sharp indenter tip. The creep study on the high entropy alloy (CoCrFeMnNi) revealed that a low stress exponent ($n = 1.3$) was obtained from nanoindentation with a spherical indenter, while it sharply rose to 28.5 with a Berkovich indenter [29], confirming that large stress exponent values are usually obtained in nanoindentation creep tests with a sharp tip, such as the Berkovich tip, which can induce high stress concentration beneath the indents.

In general, the stress exponent increases with increasing heat treatment temperature, see Fig. 5(e). In AP SCNCs, the NPs are held together by weak interactions, mainly van der Waals forces [4], making it relatively easy for the NPs to move with respect to each other, also thanks to the OA interfaces acting as a soft and somewhat flexible interlayer. When crosslinking is induced and covalent bonds are formed in heat-treated samples, instead, a higher stress is required to enable the NP movement, accounting for the increasing n values.

Strain rate sensitivity (m), the reciprocal of the stress exponent ($m = 1/n$), is an indication of the material's ability to flow viscously. The larger m, the more homogeneous the material's flow is [21]. The strain rate sensitivity, shown in Fig. 5(e), decreases with heat treatment temperature, indicating that the flow becomes progressively more inhomogeneous, and that localized shear flow can be present. The declining trend of m is another reflection of the crosslinking effect. Very low m values are associated with a quasi-perfectly-plastic behavior, as indicated in previous TEM studies on SCNCs [49].

The strain rate sensitivity is also re-examined via strain rate jump tests performed under CSM mode [38,65,66]. The goal is to verify whether the strain rate sensitivity values so obtained are comparable to those obtained via creep tests, see Fig. 5(f). Strain rate jump tests rely on lower transition times to reach prescribed strain rate values, ensuring high accuracy in the assessment of m. The tests are conducted as follows: the strain rate, controlled by $\dot{P}/2P$, drops from 2.5×10^{-2} s^{-1} to 2.5×10^{-3} s^{-1} when the displacement reaches 300 nm, and subsequently rises to 2.5×10^{-2} s^{-1} again when the displacement exceeds 400 nm. Strain rate sensitivity is then calculated as [66]

$$m = \frac{\partial ln\sigma}{\partial ln\dot{\varepsilon}} = \frac{\partial lnH}{\partial ln\dot{\varepsilon}} \tag{4}$$

where the strain rate jumps from the low value to the high one, see Fig. S7(a) and (b). The m obtained from strain rate jump tests is in good agreement, even though slightly smaller, with that from creep tests, likely due to the difference of strain rates (2–3 orders of magnitude). A fairly good agreement between the two methods is also found in the relationship between hardness and strain rates, see SI Section S9 and Fig. S7. This comparison confirms that strain rate jump tests are also a viable option to measure the strain rate sensitivity of SCNCs, with the advantage of a procedure that is less time-consuming and less impacted by thermal drift. However, strain rate jump tests are affected by a limitation when even lower strain rates are needed, due to the lower bound of loading rate characteristic of the nanoindenter [39]: a more exact m would be determined under a lower strain rate, because of the requirement of steady-state when applying Eq. (4).

6.2. Activation volume

The activation volume (V) is usually seen as an indicator of the number of atoms involved in the creep deformation process [28], and its applicability is here assessed for the case of functionalized NPs in SCNCs (the crystalline lattice in each NP undergoes negligible strains [67]). This parameter can indeed provide further insight into the creep mechanisms, and it is expressed as

$$V = kT \cdot \frac{\partial ln\dot{\gamma}}{\partial \tau} = kT \cdot \frac{\partial ln\dot{\varepsilon}}{\partial\left(\sigma/\sqrt{3}\right)} = \sqrt{3}kT \cdot \frac{\partial ln\dot{\varepsilon}}{\partial(H/3)} = 3\sqrt{3}kT \cdot \frac{\partial ln\dot{\varepsilon}}{\partial H} \tag{5}$$

where $\dot{\gamma}$ and τ are shear strain rate and strain, respectively, $\dot{\varepsilon}$ and σ are normal strain rate and strain, H is the hardness, k is Boltzmann's constant and T is the absolute temperature [29]. The shear stress τ is expressed as $\sigma/\sqrt{3}$, based on Taylor's factor relating macroscopic applied stress and shear stress in a von Mises-plasticity criterion. Based on Tabor's law, i.e. $H = C * \sigma$, C is a constraint factor that becomes ~3 in a fully plastic regime. By performing a linear fitting of logarithmic $\dot{\varepsilon}$ and linear H (SI Section S10), activation volumes are determined, as displayed in Fig. S8(a) – (d), with the corresponding values also marked in Fig. 5(a) – (d) for each load. The activation volume reduces with heat-treatment temperature in all tests. The average V values result in 0.25 nm^3 for AP SCNCs, 0.19 nm^3 for HT250, and 0.13 nm^3 for HT325. This trend confirms that crosslinking hampers creep deformation. Note that, even though both the stress exponent and the activation volume are proportional to $\frac{\partial ln\dot{\varepsilon}}{\partial H}$, for the case of the stress exponent the factor H also plays a role, and it is thus possible that the stress exponent increases while the activation volume decreases with increasing level of crosslinking.

Activation volume, at least in metals and alloys, is correlated with deformation mechanisms [68], such as plastic deformation in nanocrystalline materials [68,69], the nucleation of shear bands in metallic glasses [70], heterogeneous dislocation nucleation to account for incipient plasticity [71]. V is thus usually related to the movement of dislocations in crystalline materials. Given the materials' Burgers vector b, V can range from about 1000 b^3 (coarse grains) to several b^3 (nanocrystalline materials), and it is rationalized as the distance between obstacles during the movement of dislocations [37,66,68]. The activation volume of SCNCs (0.13 nm^3–0.25 nm^3) has values comparable to those of nanocrystalline materials (0.1 nm^3 for nanocrystalline Ni) [37,68]. But if one considers the superlattice Burgers vectors, which are extremely large at this scale (here 2 orders of magnitude larger than in atomic crystals), the SCNCs normalized activation volume, ~10^{-5} b^3, is much smaller than 1 b^3, hinting at a substantial distinction in creep deformation mechanisms with respect to the case of metals and alloys.

The creep deformation is however more in general regarded as the accumulation of activation events [71]. If an activation event is assumed to be a locally and kinetically controlled process, its frequency in a given volume can be expressed as $\dot{n} = \dot{n}_0 \cdot \exp(-\frac{Q_a - \sigma V}{kT})$, where $\dot{n}_0$ is the attempt frequency of activation event per unit volume, Q_a is the activation energy, σ is the applied stress on the activation volume V, k is the Boltzmann's constant and T is the absolute temperature [71]. The frequency of activation events then scales with the attempt frequency, hinting that in our case the duration of an activation event should be extremely short. The large deformations associated with superlattice dislocation movement are unlikely to occur in such short timeframes, but it is possible that a cumulation of shorter-range activation events

during holding (t = 1000 s) ultimately leads to superlattice dislocation movement.

Indeed, C.A. Schuh et al. found that the activation volumes corresponding to heterogeneous nucleation of dislocations ($\sim$0.5 b^3) are comparable to a vacancy volume ($\sim$0.67 b^3), thus showing that V can be smaller than 1 b^3 and that diffusion can account for small activation volumes [71]. Compared with a NP volume in SCNCs (1.7×10^3 nm^3 here), the activation volume is still smaller by 4 orders of magnitude, indicating that NPs cannot diffuse from one site to another in the superlattice during one activation event.

Considering the SCNCs' structure and constituents, a new creep mechanism is proposed to account for the extremely small normalized activation volumes. This consists of organic ligands-facilitated NP movement, achieved via the rearrangement of organic ligands in the sub-nm inter-particle spacings, such as their extension or compaction – a phenomenon which has been found to play an important role in the plastic deformation of SCNCs [49]. Even though the ID value of AP materials ($\sim$1.2 nm) suggests that ligands are interdigitated to some extent, these can still be compacted to facilitate NPs' movement. Superlattice interstitial sites can also be considered as voids here (see Results Section 1). The smaller ID in HT325 SCNCs, as well as the crosslinking, make the movement of NPs more difficult: the indentation-induced change in inter-superlattice planes spacing in AP and HT325 materials has been found to decrease from $\sim$20% to $\sim$3–4% [49,63]. Yet, such slight NP movements, which are compatible with the measured V values in SCNCs, can lead to a series of activation events contributing to the nucleation and propagation of dislocations, further facilitating viscoplastic deformation. It can then be concluded that the crosslinking of the organic ligands leads to reduced NP mobility, and thus increased resistance against creep, hampering creep deformation (Fig. 2), a phenomenon reflected in the decreasing activation volume values with increasing crosslinking level, as shown in Fig. S8.

7. Effect of testing mode: single-loading vs. CSM

The main motivation behind choosing single loading–unloading mode for this creep study is to avoid the impact of the oscillations that are an integral feature of CSM testing, although CSM exhibits the advantage of less sensitivity to thermal drift [37]. Some previous studies have demonstrated that oscillations can lead to alterations in the tested materials' behavior, such as softening in metals and hardening in polymers [46], impacting the measured values. While corrections for some of these effects have been proposed [43], SCNCs remain unexplored territory in this context: The presence of an organic phase confined in nano-sized spacings can potentially make these materials particularly sensitive to oscillations-induced alterations (e.g. organic ligands rearrangement or crosslinking). The impact of oscillations in CSM on the creep behavior of SCNCs is thus here investigated, by comparing the creep displacements obtained in single loading and CSM mode, while leaving all other testing parameters unchanged.

The creep displacements associated with CSM mode are corrected for thermal drift with two methods: the one based on contact stiffness introduced in the Appendix (see Eq. (A1) – (A5)) [37], and the one based on the same procedure used here for single loading mode (own fitting of recorded thermal drift data), see also SI Section 11. The comparison of all creep displacements (shown in Fig. S9) indicates that, when the same type of drift correction is applied, the creep displacements under CSM mode are smaller than those under single-loading mode. This trend becomes less pronounced in heat-treated materials. If, instead, the contact stiffness-based approach is adopted to determine creep displacements under CSM mode, a more marked difference emerges between the two testing modes.

It thus appears that in any case the CSM-associated oscillations do have an impact on the creep of SCNCs, leading to material hardening, even though the extent of this effect is not immediately quantifiable. Considering the constituents of SCNCs (organic ligands anchored to the inorganic NPs and confined in $\sim$1 nm interfaces) and the CSM oscillations amplitude (2 nm, larger than interparticle distances), oscillation-induced hardening can indeed occur. This is somewhat analogous to the storage modulus of polymers increasing with frequency in mechanical testing [72,73]. Nanoindentation also leads to material compaction [17], which can lead to the stiffening of the material, make it the CSM assumption of constant elastic modulus not fully applicable in this context. Further details on this analysis are given SI Section S11. The use of single-loading mode is thus confirmed to be suitable for this particular type of hybrid nanomaterials, to rule out any oscillation-induced material alterations, even though the assessment of thermal drift stays an important aspect to carefully tackle in long-term nanoindentation testing. Strain rate jump tests are a instead a viable option for strain rate sensitivity analysis.

8. Conclusions

The creep behavior of ceramic-organic supercrystalline nanocomposites (SCNCs), consisting of iron oxide NPs functionalized with oleic acid, has been investigated via nanoindentation, together with the effect of oscillations in continuous stiffness measurement (CSM) on the same creep deformation. The main findings are the following:

1) Creep occurs in SCNCs, both in presence and absence of crosslinking of the organic phase. Heat-treated (crosslinked) samples show a higher resistance against creep, reflected by smaller overall creep displacements. Creep recovery also occurs, but not completely even several weeks after nanoindentation, implying that viscoelasticity and viscoplasticity are both part of the creep deformation.

2) Initial creep dominates the total creep deformation, due to a higher deformation rate at the onset of creep.

3) During quasi-secondary creep, a large stress exponent ($n > 7$) hints at the occurrence of power-law breakdown in SCNCs, an effect that is also verified by comparing threshold stress values to trigger power-law breakdown and representative under-indent stress. The increasing stress exponents with heat treatment temperature are also ascribed to the enhancement of mechanical properties induced by the crosslinking.

4) The extremely small normalized activation volumes with respect to the superlattices Burgers vector ($\sim 10^{-5}$ b^3) are interpreted as associated with slight NP movements, facilitated by rearrangement of the organic ligands in the superlattice, which are hindered when surface ligands are crosslinked.

5) Comparable strain rate sensitivity values are obtained from creep tests and strain rate jump tests.

Even though ligands only occupy a minor fraction of the SCNCs, this marked creep behavior is a clear signal of their strong influence on the nanocomposites' mechanical behavior, an effect that is tunable via crosslinking of the organic phase, which alters the NP-NP interactions. Additional control knobs to tailor the mechanical behavior of this new category of inorganic–organic nanocomposite materials can be identified in the NP size and shape and especially in the ligand density, length and characteristic backbone. Many potential research avenues can be pursued to enable the implementation of SCNCs in a plethora of different applications.

Data availability

Data will be made available on request.

Declaration of Competing Interest

The authors declare that they have no known competing financial interests or personal relationships that could have appeared to influence the work reported in this paper.

Acknowledgements

The authors gratefully acknowledge the financial support from the Deutsche Forschungsgemeinschaft (DFG, German Research Foundation), project numbers GI 1471/1-1 and 192346071-SFB 986. The authors are thankful to Fraunhofer CAN GmbH for the TEM images of the functionalized nanoparticles, Prof. Gerold Schneider (Hamburg University of Technology) for the fruitful discussion, Dr. Jasmin Koldehoff (Hamburg University of Technology) for the assistance with nanoindentation tests, Dr. Hans Jelitto (Hamburg University of Technology) for the assistance with AFM measurements, and Dr. Emad Maawad (Institute of Materials Physics, Helmholtz-Zentrum Hereon) for assistance with the SAXS data acquisition.

Appendix A

Due to the long holding time and low deformation rates in this creep study, the impact of thermal drift cannot be neglected. The contact stiffness is, however, less sensitive to thermal drift, and Maier et al. proposed a method to calculate indentation displacements based on contact stiffness, here summarized [37].

From Sneddon's equation,

$$S = \frac{2\beta}{\sqrt{\pi}} \cdot E_R \cdot \sqrt{A_c} \tag{A1}$$

where S is the harmonic contact stiffness measured via nanoindentation, β is a correction factor accounting for the indenter's shape that has a value of 1.05 for the Berkovich tip [22], E_R is the reduced modulus and A_c is the contact area.

The reduced modulus E_R is calculated from

$$\frac{1}{E_R} = \frac{1-\nu_s^2}{E_s} + \frac{1-\nu_i^2}{E_i} \tag{A2}$$

where the subscripts s and i denote sample and indenter; E and ν elastic modulus and Poisson's ratio, respectively.

With Eq. (A.1) and (A.2), the contact area A_c can be obtained as

$$A_c = \frac{\pi}{4\beta^2} \cdot \frac{S^2}{E_R^2} \tag{A3}$$

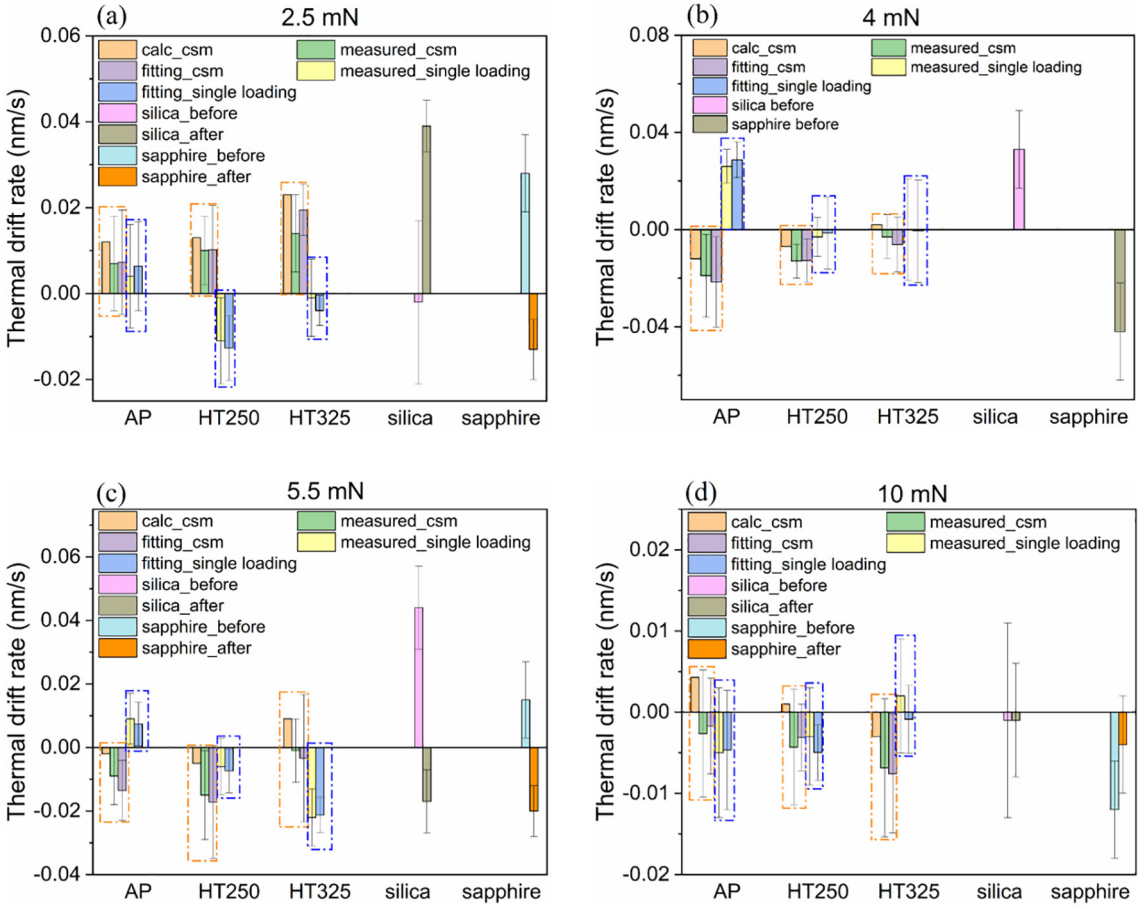

Fig. A1. Comparison of thermal drift rates obtained with different methods, for test under: (a) 2.5 mN; (b) 4 mN; (c) 5.5 mN; (d) 10 mN. The thermal drift rates measured under CSM mode are marked by orange dashed rectangles, while those under single loading mode are marked by blue dashed rectangles. The other data is relative to silica and sapphire. The latter are missing for the after-creep stage in the 4 mN tests, due to an unforeseen interruption of the testing cycles after the creep measurements. (For interpretation of the references to colour in this figure legend, the reader is referred to the web version of this article.)

The contact area function of indenter is calibrated on silica, and it is found to be:

$$A_c = 24.5h_c^2 + 249.52h_c + 173.4h_c^{0.5} + 78.91h_c^{0.25} + 51.87h_c^{0.125} \quad (A4)$$

By numerically solving eq. (A.4), the value of contact depth h_c can be obtained. The total displacement can then be calculated as

$$h_{csm} = h_c + \varepsilon \cdot \frac{P}{S} \quad (A5)$$

where ε is a constant depending on the geometry of the indenter, which has a value of 0.75 for Berkovich tip [74].

The difference between h_{csm} and h_{meas} (raw nanoindentation data) is ascribed to the effect of thermal drift:

$$h_{thermal} = h_{meas} - h_{csm} \quad (A6)$$

The time derivative of $h_{thermal}$ is the thermal drift:

$$\lambda = dh_{thermal}/dt \quad (A7)$$

We compare the resulting thermal drift with the one resulting from alternative approaches. These are: (i) the thermal drift data measured by the nanoindenter itself, as fitted by the device or with an own, more accurate, fit, and (ii) the thermal drift data resulting from indenting reference materials for which the creep deformation is either known or negligible, namely silica and sapphire. All these options are evaluated for their suitability to our tests, and the most appropriate is then selected and applied to the creep data.

More specifically, the following thermal drift assessment methods are implemented and evaluated. The resuting drift rates obtained are compared in Fig. A1.

Under CSM mode:

a) drift calculated based on the measured contact stiffness (calc_csm in the plot);

b) drift provided by the nanoindenter based on the dedicated segment in the tests (measured_csm);

c) own fitting (fitting_csm) of the data of (b);

d) data extracted by silica tests;

e) data extracted by sapphire tests.

Under single loading mode:

f) data provided by the nanoindenter based on the dedicated segment in the tests (measured_single loading);

g) own fitting (fitting_single loading) of the data of (f).

Under CSM mode, the drift values relative to silica and sapphire are not consistent before (silica/sapphire_before in the plot) and after creep tests (silica/sapphire_after in the plot) for the 2.5 mN and 5.5 mN tests, and they are not comparable to those from Eq. (A.7). This drift data is thus discarded. The drift values based on the nanoindenter measurement and on own linear fitting are comparable, and they are also comparable to those from Eq. (A.7), indicating that this data can be employed for the correction.

Under single loading mode, the drift values from measurement of nanoindentation and own linear fitting are also comparable, but the drift values from Eq. (A.7) under CSM mode significantly deviate from these in certain tests. Therefore, the value from Eq. (A.7) is not used here to correct the raw data obtained under single loading mode.

Based on these considerations, the data obtained from the thermal drift measurements will be adopted for the correction of the raw data measured in single loading mode, with an own fitting applied to improve accuracy (g), while for CSM mode both the contact-stiffness based method (a) and the same procedure adopted to correct the single loading data (c) are applied.

Appendix B. Supplementary data

Supplementary data to this article can be found online at https://doi.org/10.1016/j.matdes.2023.112000.

References

[1] M.R. Begley, D.S. Gianola, T.R. Ray, Bridging functional nanocomposites to robust macroscale devices, Science 364 (2019) eaav4299, https://doi.org/10.1126/science.aav4299.

[2] E.V. Sturm, H. Cölfen, Mesocrystals: past, presence, future, Crystals 7 (2017) 207, https://doi.org/10.3390/cryst7070207.

[3] M.A. Boles, M. Engel, D.V. Talapin, Self-assembly of colloidal nanocrystals: From intricate structures to functional materials, Chem. Rev. 116 (2016) 11220–11289, https://doi.org/10.1021/acs.chemrev.6b00196.

[4] A. Dreyer, A. Feld, A. Kornowski, E.D. Yilmaz, H. Noei, A. Meyer, T. Krekeler, C. Jiao, A. Stierle, V. Abetz, H. Weller, G.A. Schneider, Organically linked iron oxide nanoparticle supercrystals with exceptional isotropic mechanical properties, Nat. Mater. 15 (2016) 522–528, https://doi.org/10.1038/nmat4553.

[5] E. Tam, P. Podsiadlo, E. Shevchenko, D.F. Ogletree, M.P. Delplancke-Ogletree, P. D. Ashby, Mechanical properties of face-centered cubic supercrystals of nanocrystals, Nano Lett. 10 (2010) 2363–2367, https://doi.org/10.1021/nl1001313.

[6] L. Bergström, E.V. Sturm (née Rosseeva), G. Salazar-Alvarez, H. Cölfen, Mesocrystals in biominerals and colloidal arrays, Acc. Chem. Res. 48 (5) (2015) 1391–1402.

[7] M.P. Pileni, Nanocrystal self-assemblies: fabrication and collective properties, J. Phys. Chem. B 105 (2001) 3358–3371, https://doi.org/10.1021/jp0039520.

[8] T. Tachikawa, T. Majima, Metal oxide mesocrystals with tailored structures and properties for energy conversion and storage applications, NPG Asia Mater. 6 (5) (2014) e100–e.

[9] Z. Tang, N.A. Kotov, S. Magonov, B. Ozturk, Nanostructured artificial nacre, Nat. Mater. 2 (2003) 413–418, https://doi.org/10.1038/nmat906.

[10] F. Bouville, E. Maire, S. Meille, B. van de Moortèle, A.J. Stevenson, S. Deville, Strong, tough and stiff bioinspired ceramics from brittle constituents, Nat. Mater. 13 (2014) 508–514, https://doi.org/10.1038/nmat3915.

[11] M.P. Pileni, Mechanical properties of supracrystals, EPL. 119 (2017) 37002, https://doi.org/10.1209/0295-5075/119/37002.

[12] X.W. Gu, Mechanical properties of architected nanomaterials made from organic-inorganic nanocrystals, JOM. 70 (2018) 2205–2217, https://doi.org/10.1007/s11837-018-3094-7.

[13] P. Podsiadlo, G. Krylova, B. Lee, K. Critchley, D.J. Gosztola, D.V. Talapin, P.D. Ashby, E.V. Shevchenko, The role of order, nanocrystal size, and capping ligands in the collective mechanical response of three-dimensional nanocrystal solids, J. Am. Chem. Soc. 132 (26) (2010) 8953–8960.

[14] B. Domènech, A. Plunkett, M. Kampferbeck, M. Blankenburg, B. Bor, D. Giuntini, T. Krekeler, M. Wagstaffe, H. Noei, A. Stierle, M. Ritter, M. Müller, T. Vossmeyer, H. Weller, G.A. Schneider, Modulating the mechanical properties of supercrystalline nanocomposite materials via solvent-ligand interactions, Langmuir. 35 (2019) 13893–13903, https://doi.org/10.1021/acs.langmuir.9b01938.

[15] M. Gauvin, N. Yang, Z. Yang, I. Arfaoui, M.P. Pileni, Hierarchical mechanical behavior of cobalt supracrystals related to nanocrystallinity, Nano Res. 8 (2015) 3480–3487, https://doi.org/10.1007/s12274-015-0846-3.

[16] M. Gauvin, N. Yang, E. Barthel, I. Arfaoui, J. Yang, P.A. Albouy, M.P. Pileni, Morphology, nanocrystallinity, and elastic properties of single domain ε Co supracrystals, J. Phys. Chem. C 119 (2015) 7483–7490, https://doi.org/10.1021/acs.jpcc.5b00358.

[17] B. Bor, D. Giuntini, B. Domènech, M.V. Swain, G.A. Schneider, Nanoindentation-based study of the mechanical behavior of bulk supercrystalline ceramic-organic nanocomposites, J. Eur. Ceram. Soc. 39 (2019) 3247–3256, https://doi.org/10.1016/j.jeurceramsoc.2019.03.053.

[18] B. Bor, D. Giuntini, B. Domènech, A. Plunkett, M. Kampferbeck, T. Vossmeyer, H. Weller, I. Scheider, G.A. Schneider, Constitutive and fracture behavior of ultra-strong supercrystalline nanocomposites, Appl. Phys. Rev. 8 (3) (2021) 031414.

[19] A. Plunkett, M. Kampferbeck, B. Bor, U. Sazama, T. Krekeler, L. Bekaert, H. Noei, D. Giuntini, M. Fröba, A. Stierle, H. Weller, T. Vossmeyer, G.A. Schneider, B. Domènech, Strengthening engineered nanocrystal three-dimensional superlattices via ligand conformation and reactivity, ACS Nano. 16 (2022) 11692–11707, https://doi.org/10.1021/acsnano.2c01332.

[20] K.S. Sugi, P. Bandyopadhyay, M. Bodiuzzaman, A. Nag, M. Hridya, W.A. Dar, P. Ghosh, T. Pradeep, Manifestation of structural differences of atomically precise cluster-assembled solids in their mechanical properties, Chem. Mater. 32 (2020) 7973–7984, https://doi.org/10.1021/acs.chemmater.0c02905.

[21] L.H. He, M.V. Swain, Nanoindentation creep behavior of human enamel, J. Biomed. Mater. Res. A 91 (2009) 352–359, https://doi.org/10.1002/jbm.a.32223.

[22] J. Menčík, L.H. He, M.V. Swain, Determination of viscoelastic-plastic material parameters of biomaterials by instrumented indentation, J. Mech. Behav. Biomed. Mater. 2 (2009) 318–325, https://doi.org/10.1016/j.jmbbm.2008.09.002.

[23] Z. Wu, T.A. Baker, T.C. Ovaert, G.L. Niebur, The effect of holding time on nanoindentation measurements of creep in bone, J. Biomech. 44 (2011) 1066–1072, https://doi.org/10.1016/j.jbiomech.2011.01.039.

[24] A.J. van der Veen, A. Bisschop, M.G. Mullender, J.H. van Dieën, Modelling creep behaviour of the human intervertebral disc, J. Biomech. 46 (2013) 2101–2103, https://doi.org/10.1016/j.jbiomech.2013.05.026.
[25] S.N.G. Chu, J.C.M. Li, Impression creep; a new creep test, J. Mater. Sci. 12 (1977) 2200–2208, https://doi.org/10.1007/BF00552241.
[26] I.C. Choi, B.G. Yoo, Y.J. Kim, M.Y. Seok, Y. Wang, J. il Jang, Estimating the stress exponent of nanocrystalline nickel: sharp vs. spherical indentation, Scr. Mater. 65 (2011) 300–303, https://doi.org/10.1016/j.scriptamat.2011.04.031.
[27] C.L. Wang, Y.H. Lai, J.C. Huang, T.G. Nieh, Creep of nanocrystalline nickel: A direct comparison between uniaxial and nanoindentation creep, Scr. Mater. 62 (2010) 175–178, https://doi.org/10.1016/j.scriptamat.2009.10.021.
[28] C.L. Wang, M. Zhang, T.G. Nieh, Nanoindentation creep of nanocrystalline nickel at elevated temperatures, J. Phys. D: Appl. Phys. 42 (11) (2009) 115405.
[29] D.H. Lee, M.Y. Seok, Y. Zhao, I.C. Choi, J. He, Z. Lu, J.Y. Suh, U. Ramamurty, M. Kawasaki, T.G. Langdon, J. il Jang, Spherical nanoindentation creep behavior of nanocrystalline and coarse-grained CoCrFeMnNi high-entropy alloys, Acta Mater. 109 (2016) 314–322, https://doi.org/10.1016/j.actamat.2016.02.049.
[30] R. Machaka, T.E. Derry, I. Sigalas, Room temperature nanoindentation creep of hot-pressed B6O, Mater. Sci. Eng. A 607 (2014) 521–524, https://doi.org/10.1016/j.msea.2014.04.035.
[31] N. Janakiraman, F. Aldinger, Yielding, strain hardening, and creep under nanoindentation of precursor-derived si-C-N ceramics, J. Am. Ceram. Soc. 93 (2010) 821–829, https://doi.org/10.1111/j.1551-2916.2009.03491.x.
[32] C. Su, E.G. Herbert, S. Sohn, J.A. LaManna, W.C. Oliver, G.M. Pharr, Measurement of power-law creep parameters by instrumented indentation methods, J. Mech. Phys. Solids 61 (2013) 517–536, https://doi.org/10.1016/j.jmps.2012.09.009.
[33] C.C. Huang, M.K. Wei, S. Lee, Transient and steady-state nanoindentation creep of polymeric materials, Int. J. Plast. 27 (2011) 1093–1102, https://doi.org/10.1016/j.ijplas.2010.11.005.
[34] R. Goodall, T.W. Clyne, A critical appraisal of the extraction of creep parameters from nanoindentation data obtained at room temperature, Acta Mater. 54 (2006) 5489–5499, https://doi.org/10.1016/j.actamat.2006.07.020.
[35] P.S. Phani, W.C. Oliver, A direct comparison of high temperature nanoindentation creep and uniaxial creep measurements for commercial purity aluminum, Acta Mater. 111 (2016) 31–38, https://doi.org/10.1016/j.actamat.2016.03.032.
[36] J.B. Pethica, W.C. Oliver, Tip surface interactions in STM and AFM, Phys. Scr. 19 (1987) 61–66, https://doi.org/10.1088/0031-8949/1987/T19A/010.
[37] V. Maier, B. Merle, M. Göken, K. Durst, An improved long-term nanoindentation creep testing approach for studying the local deformation processes in nanocrystalline metals at room and elevated temperatures, J. Mater. Res. 28 (2013) 1177–1188, https://doi.org/10.1557/jmr.2013.39.
[38] V. Maier, A. Leitner, R. Pippan, D. Kiener, Thermally Activated Deformation Behavior of ufg-Au: Environmental Issues During Long-Term and High-Temperature Nanoindentation Testing, JOM. 67 (2015) 2934–2944, https://doi.org/10.1007/s11837-015-1638-7.
[39] K. Durst, V. Maier, Dynamic nanoindentation testing for studying thermally activated processes from single to nanocrystalline metals, Curr. Opin. Solid State Mater. Sci. 19 (2015) 340–353, https://doi.org/10.1016/j.cossms.2015.02.001.
[40] X. Li, B. Bhushan, A review of nanoindentation continuous stiffness measurement technique and its applications, Mater. Charact. 48 (2002) 11–36, https://doi.org/10.1016/S1044-5803(02)00192-4.
[41] K. Diehl, T. Staedler, X. Jiang, Accessing fatigue information by means of dynamic nanoindentation, Appl. Phys. Lett. 114 (21) (2019) 213101.
[42] X. Li, B. Bhushan, Nanofatigue studies of ultrathin hard carbon overcoats used in magnetic storage devices, J. Appl. Phys. 91 (2002) 8334–8336, https://doi.org/10.1063/1.1452699.
[43] G.M. Pharr, J.H. Strader, W.C. Oliver, Critical issues in making small-depth mechanical property measurements by nanoindentation with continuous stiffness measurement, J. Mater. Res. 24 (2009) 653–666, https://doi.org/10.1557/jmr.2009.0096.
[44] B. Merle, V. Maier-Kiener, G.M. Pharr, Influence of modulus-to-hardness ratio and harmonic parameters on continuous stiffness measurement during nanoindentation, Acta Mater. 134 (2017) 167–176, https://doi.org/10.1016/j.actamat.2017.05.036.
[45] S.J. Vachhani, R.D. Doherty, S.R. Kalidindi, Effect of the continuous stiffness measurement on the mechanical properties extracted using spherical nanoindentation, Acta Mater. 61 (2013) 3744–3751, https://doi.org/10.1016/j.actamat.2013.03.005.
[46] M.J. Cordill, N.R. Moody, W.W. Gerberich, Effects of dynamic indentation on the mechanical response of materials, J. Mater. Res. 23 (2008) 1604–1613, https://doi.org/10.1557/jmr.2008.0205.
[47] K.W. Siu, A.H.W. Ngan, The continuous stiffness measurement technique in nanoindentation intrinsically modifies the strength of the sample, Philos. Mag. 93 (2013) 449–467, https://doi.org/10.1080/14786435.2012.722234.
[48] M.J. Cordill, M.S. Lund, J. Parker, C. Leighton, A.K. Nair, D. Farkas, N.R. Moody, W.W. Gerberich, The Nano-Jackhammer effect in probing near-surface mechanical properties, Int. J. Plast. 25 (2009) 2045–2058, https://doi.org/10.1016/j.ijplas.2008.12.015.
[49] D. Giuntini, S. Zhao, T. Krekeler, M. Li, M. Blankenburg, B. Bor, G. Schaan, B. Domènech, M. Müller, I. Scheider, M. Ritter, G.A. Schneider, Defects and plasticity in ultrastrong supercrystalline nanocomposites, Sci. Adv. 7 (2021), https://doi.org/10.1126/sciadv.abb6063.
[50] E.R. Garland, E.P. Rosen, L.I. Clarke, T. Baer, Structure of submonolayer oleic acid coverages on inorganic aerosol particles: Evidence of island formation, Phys. Chem. Chem. Phys. 10 (2008) 3156–3161, https://doi.org/10.1039/b718013f.
[51] M. Rudolph, J. Erler, U.A. Peuker, A TGA-FTIR perspective of fatty acid adsorbed on magnetite nanoparticles-Decomposition steps and magnetite reduction, Colloids Surf. A 397 (2012) 16–23, https://doi.org/10.1016/j.colsurfa.2012.01.020.
[52] C.A. Tweedie, K.J. van Vliet, Contact creep compliance of viscoelastic materials via nanoindentation, J. Mater. Res. 21 (2006) 1576–1589, https://doi.org/10.1557/jmr.2006.0197.
[53] S. Yang, Y.W. Zhang, K. Zeng, Analysis of nanoindentation creep for polymeric materials, J. Appl. Phys. 95 (2004) 3655–3666, https://doi.org/10.1063/1.1651341.
[54] F. Alvarez, A. Alegria, J. Colmenero, Relationship between the time-domain Kohlrausch-Williams-Watts and frequency-domain Havriliak-Negami relaxation functions, Phys Rev B. 44 (1991) 7306–7312, https://doi.org/10.1103/PhysRevB.44.7306.
[55] R.S. Mishra, D. Banerjee, Transient mechanisms in diffusional creep in a titanium alumnide, Scr. Metall. Mater. 31 (1994) 1555–1560, https://doi.org/10.1016/0956-716X(94)90073-6.
[56] T. Neeraj, D.-H. Hou, G.S. Daehn, M.J. Mills, Phenomenological and microstructural analysis of room temperature creep in titanium alloys, Acta Mater. 48 (2000) 1225–1238, https://doi.org/10.1016/S1359-6454(99)00426-7.
[57] W.B. Li, J.L. Henshall, R.M. Hooper, K.E. Easterling, The mechanisms of indentation creep, Acta Metall. Mater. 39 (1991) 3099–3110, https://doi.org/10.1016/0956-7151(91)90043-Z.
[58] T.G. Langdon, Grain boundary sliding revisited: Developments in sliding over four decades, J. Mater. Sci. 41 (2006) 597–609, https://doi.org/10.1007/s10853-006-6476-0.
[59] P. Yavari, T.G. Langdon, An examination of the breakdown in creep by viscous glide in solid solution alloys at high stress levels, Acta Metall. 30 (1982) 2181–2196, https://doi.org/10.1016/0001-6160(82)90139-0.
[60] C.D. Gu, J.S. Lian, Q. Jiang, W.T. Zheng, Experimental and modelling investigations on strain rate sensitivity of an electrodeposited 20 nm grain sized Ni, J. Phys. D: Appl. Phys. 40 (2007) 7440–7446, https://doi.org/10.1088/0022-3727/40/23/027.
[61] M.E. Kassner, R. Ermagan, Power law breakdown in the creep in single-phase metals, Metals 9 (2019) 1345, https://doi.org/10.3390/met9121345.
[62] G.M. Pharr, Some observations on the relation between dislocation substructure and power law breakdown, Scr. Metall. 15 (1981) 713–717, https://doi.org/10.1016/0036-9748(81)90005-3.
[63] M. Li, I. Scheider, B. Bor, B. Domènech, G.A. Schneider, D. Giuntini, Ultra-thin and ultra-strong organic interphase in nanocomposites with supercrystalline particle arrangement: Mechanical behavior identification via multiscale numerical modeling, Compos. Sci. Technol. 198 (2020), https://doi.org/10.1016/j.compscitech.2020 108283.
[64] K.L. Johnson, K.L. Johnson, Contact Mechanics, Cambridge University Press, 1987.
[65] J. May, H.W. Höppel, M. Göken, Strain rate sensitivity of ultrafine-grained aluminium processed by severe plastic deformation, Scr. Mater. 53 (2005) 189–194, https://doi.org/10.1016/j.scriptamat.2005.03.043.
[66] Q. Wei, S. Cheng, K.T. Ramesh, E. Ma, Effect of nanocrystalline and ultrafine grain sizes on the strain rate sensitivity and activation volume: Fcc versus bcc metals, Mater. Sci. Eng. A 381 (2004) 71–79, https://doi.org/10.1016/j.msea.2004.03.064.
[67] D. Giuntini, A. Davydok, M. Blankenburg, B. Domènech, B. Bor, M. Li, I. Scheider, C. Krywka, M. Müller, G.A. Schneider, Deformation Behavior of Cross-Linked Supercrystalline Nanocomposites: An in Situ SAXS/WAXS Study during Uniaxial Compression, Nano Lett. 21 (2021) 2891–2897, https://doi.org/10.1021/acs.nanolett.0c05041.
[68] Y. Wang, A. Hamza, E. Ma, Temperature-dependent strain rate sensitivity and activation volume of nanocrystalline Ni, Acta Mater. 54 (10) (2006) 2715–2726.
[69] R.J. Asaro, S. Suresh, Mechanistic models for the activation volume and rate sensitivity in metals with nanocrystalline grains and nano-scale twins, Acta Mater. 53 (2005) 3369–3382, https://doi.org/10.1016/j.actamat.2005.03.047.
[70] L. Perrière, S. Nowak, S. Brossard, M.T. Thai, M. Blétry, Y. Champion, Nanoindentation study of chemical effects on the activation volume controlling shear band initiation in metallic glasses, Scr. Mater. 68 (2013) 183–186, https://doi.org/10.1016/j.scriptamat.2012.10.013.
[71] C.A. Schuh, J.K. Mason, A.C. Lund, Quantitative insight into dislocation nucleation from high-temperature nanoindentation experiments, Nat. Mater. 4 (2005) 617–621, https://doi.org/10.1038/nmat1429.
[72] C. Chindam, A. Lakhtakia, N.R. Brown, W. Orfali, O.O. Awadelkarim, Frequency- and temperature-dependent storage and loss moduli of microfibrous thin films of Parylene C, Mater. Lett. 116 (2014) 296–298, https://doi.org/10.1016/j.matlet.2013.11.054.
[73] X. Xu, S.H.R. Sanei, E. Steinmetz, A. Gohn, J. Williams, Effect of microstructure uncertainty and testing frequency on storage and loss moduli of injection molded MWCNT reinforced polyamide 66 nanocomposites, Polym. Test. 85 (2020) 106455.
[74] B. Merle, V. Maier, M. Göken, K. Durst, Experimental determination of the effective indenter shape and ε-factor for nanoindentation by continuously measuring the unloading stiffness, J. Mater. Res. 27 (2012) 214–221, https://doi.org/10.1557/jmr.2011.245.